Effects of Multiple Platinum Species on Catalytic Reactivity Distinguished by Electron Microscopy and X-ray Absorption Spectroscopy Techniques

Bing Nan,[†,‡] Xiu-Cui Hu,[∥] Xu Wang,[‡] Chun-Jiang Jia,*[,∥] Chao Ma,*[,§] Ming-Xing Li,[†] and Rui Si*[,‡]
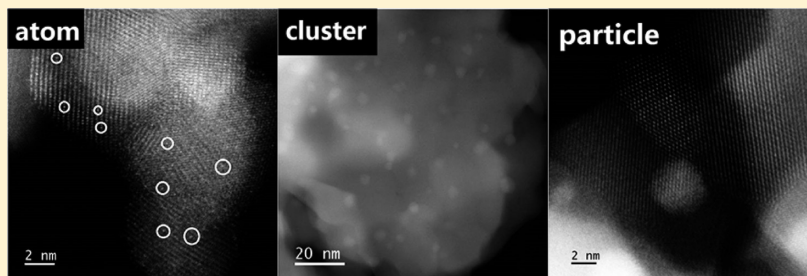
[†]Department of Chemistry, College of Science, Shanghai University, Shanghai 200444, China

[‡]Shanghai Synchrotron Radiation Facility, Shanghai Institute of Applied Physics, Chinese Academy of Sciences, Shanghai 201204, China

[∥]Key Laboratory for Colloid and Interface Chemistry, Key Laboratory of Special Aggregated Materials, School of Chemistry and Chemical Engineering, Shandong University, Jinan 250100, China

[§]Center for High Resolution Electron Microscopy, College of Materials Science and Engineering, Hunan University, Changsha 410082, China

S *Supporting Information*

ABSTRACT: Supported platinum species in the forms of single atoms, ultrafine clusters, and metallic particles have been widely investigated because of their unique catalytic properties in diverse redox reactions. In this work, we used thermally stable ceria–zirconia–lanthana ($Ce_{0.5}Zr_{0.42}La_{0.08}O_x$) as an active oxide support to deposit platinum with different loading amounts from 0.5 to 2 at. % via an incipient wetness impregnation. The as-obtained samples were measured under the methane oxidation reaction conditions with high space velocities up to 100,000 $mL \cdot g^{-1} \cdot h^{-1}$. Here, 1 at. % Pt sample showed the best catalytic performance with a total reaction rate of 1.93 $\mu mol_{CH4} \cdot g_{cat}^{-1} \cdot s^{-1}$ and exclusive platinum rate of 24.4 $mmol_{CH4} \cdot mol_{Pt}^{-1} \cdot s^{-1}$ at 450 °C. Multiple characterization means, especially aberration-corrected high-angle annular dark-field scanning transmission electron microscopy (HAADF-STEM) and X-ray absorption fine structure (XAFS) with the related profile fittings, were carried out to determine the electronic and local coordination structures of platinum. On the basis of these experimental evidence, we have distinguished the effects of different components and found that platinum oxide clusters (Pt_xO_y) with averaged sizes from subnanometer to 2−3 nm play an essential role for the oxidation of methane. Metallic Pt particles are probably active species, but their large-size characteristics impair the reactivity. However, ionic platinum single atoms may not be appropriate for this catalytic process.

1. INTRODUCTION

Natural gas, which consists primarily of methane, had been receiving much attention because of its nonpollution status, abundant reserves, and environmentally friendliness.[1,2] Catalytic oxidation of methane is an efficient technology that could be used for removal of hydrocarbons from automobile gas exhaust or as heat sources in boilers or stoves.[3] The active component for oxidation of methane has been focused on noble metals (Pt,[4,11,20] Pd,[5,12] Rh,[6] and Au[2,7]) and transition metal oxides (Ni,[8] Co,[9] and Cu[10]). Although the transition metal oxide catalysts are less expensive, they generally show lower catalytic activity and higher light-off temperature than the noble metal ones.[11] Among noble metals, palladium is the most commonly used and studied catalyst, exhibiting extremely high activity (e.g., complete conversion of methane below 400 °C).[12] However, the platinum catalysts

seemed to be inactive for the total oxidation of methane at low temperatures less than 400 °C,[13,20] probably due to the extremely limited studies on the active Pt species as well as the structure–activity relationship.[14,15]

Since the 1970s, investigations of the size effect of metal,[15] the support effect of the oxide matrix,[16] the nature of the active species,[14] and the metal–support interactions[17] have been carried out on the metal oxide-supported platinum catalysts for the oxidation of methane. For example, Persson et al. deposited bimetallic Pd–Pt on the various support materials that showed the distinct activity at different temperature ranges.[16] Tang et al.

25805

prepared the Pt/CeO$_2$ catalyst by three methods, photoassisted deposition-precipitation, sol−gel, and flame combustion and found that the activity improved as the fraction of ionic Pt increased.[14] However, until now, there are still debates about the origin of the reactivity of platinum-based catalysts, and multiple active sites (single atoms,[18] ultrafine clusters,[19] and nano-particles[20]) or different oxidation states of Pt (metallic[21] and ionic[14]) have been proposed previously. The difficulty is mainly due to the complexity of supported Pt structures, which requires the development of effective structural characterization methods for the comprehensive detection of these platinum species at the atomic level.

Taking the high temperature of oxidation of methane into consideration, not only the platinum active phase but also the metal oxide support should have high thermal stability (e.g., up to 600−700 °C). Ceria (CeO$_2$) is one of the most important functional rare-earth oxides and has received remarkably increasing research interest due to its excellent oxygen storage capacity and ability to disperse precious metal species.[22−25] However, when the catalytic reaction happens at elevated temperature above 500−600 °C, CeO$_2$ will undergo sintering and become huge particles, which results in the serious deactivation on the supported metals. Therefore, many research groups have devoted themselves to synthesizing divalent doped-ceria (e.g., CeO$_2$−ZrO$_2$)[26] or trivalent doped-ceria (e.g., CeO$_2$−ZrO$_2$−RE$_2$O$_3$, RE = La, Pr, Nd, Y)[27] with high chemical and structural homogeneity.

However, due to the complexity in structure of small-size metal/metal oxide species such as single atoms, ultrafine clusters, and large particles, advanced characterization techniques are required to precisely detect the electronic and local coordination structures around the active metal center. Among them, aberration-corrected high-angle annular dark-field scanning transmission electron microscopy (HAADF-STEM)[28,29] and X-ray absorption fine structure (XAFS)[30,31] play crucial roles in determining these species at the atomic scale, either giving microscopic direct observations or providing macroscopic averaged structural information. Li et al. quantitatively described the complex structural dynamics of supported Pt catalysts during ethylene hydrogenation by the help of synchrotron X-ray absorption spectroscopy and scanning transmission electron microscopy in operando conditions.[30]

Previously, trivalent ceria−zirconia−lanthana solid solutions prepared by urea-based hydrolysis with the help of hydrothermal treatment have been demonstrated to have good thermal stability, keeping a single-phase structure even after calcined in air at 1000 °C for 100 h.[27] Herein, we report the preparation of platinum-doped ceria−zirconia−lanthana (Pt−Ce$_{0.5}$Zr$_{0.42}$La$_{0.08}$O$_{2−x}$) catalysts via the sequential incipient wetness impregnation to the as-calcined oxide support, as well as their catalytic performance for the oxidation of methane in the range of 300−650 °C. By the aids of HAADF-STEM and XAFS techniques, we found that multiple platinum species, such as ultrafine clusters and nano-particles, formed during synthesis and were stabilized under the reaction conditions. On the basis of the obtained structural information, we also determined the specific contribution of multiple platinum species, including ionic platinum single atoms, ultrafine platinum oxide clusters, and metallic Pt large particles for the methane oxidation reaction.

2. EXPERIMENTAL SECTION

2.1. Catalyst Preparation. All of the chemicals applied to our experiments are of analytical grade and were used without further purification or modification. Ammonium cerium(IV)

nitrate ((NH$_4$)$_2$Ce(NO$_3$)$_6$, ≥99.0%)), lanthanum(III) nitrate hydrate (La(NO$_3$)$_3$·H$_2$O, AR), and urea (CON$_2$H$_4$, ≥99.0%)) were purchased from Sinopharm Chemical Reagent Co., Ltd. Zirconium(IV) oxynitrate hydrate (ZrO(NO$_3$)$_2$·H$_2$O, 99.5%) was obtained from Aladdin Industrial Corporation. Tetra-ammineplatinum(II) nitrate (Pt(NH$_3$)$_4$(NO$_3$)$_2$, 99.99%) was purchased from Alfa Aesar Chemical Reagent Co., Ltd.

Ce$_{0.5}$Zr$_{0.42}$La$_{0.08}$O$_2$ (**CZL**) supports were prepared by the method that has been reported previously.[27] In the initial step, (NH$_4$)$_2$Ce(NO$_3$)$_6$, ZrO(NO$_3$)$_2$·H$_2$O, La(NO$_3$)$_3$·H$_2$O, and urea in the molar ratio of 0.5:0.42:0.08:6 were dissolved in 70 mL of deionized water with the total metal concentration of 0.1 mol L^{-1} and stirred for 1 h at room temperature. Then, the stock solution was transferred into a Teflon bottle (inner volume: 100 mL), which was kept in a stainless-steel autoclave. After the autoclave was sealed tightly, it was placed in a temperature-controlled electric oven. The vessel was heated to 80 °C within 0.5 h and then kept for another 6 h. The temperature of the vessel was sequentially raised to 180 °C within 1 h and was kept for another 24 h. After the hydrothermal process finished and the vessel was cooled down to room temperature, the as-obtained precipitates were separated by centrifugation and washed with deionized water and ethanol several times until neutral (pH = 7). The as-washed products were dried at 80 °C in still air for 12 h, thoroughly grounded, and then calcined at 800 °C for 4 h (ramping rate: 2 °C/min).

Deposition of platinum onto the as-calcined **CZL** support was carried out by an incipient wetness impregnation (IMP). The atomic percentage of Pt was designed to be 0.5, 1.0, and 2.0 at. %, which was denoted as **0.5Pt-CZL**, **1Pt-CZL**, and **2Pt-CZL**, respectively. Aqueous solution of Pt(NH$_3$)$_4$(NO$_3$)$_2$ (12.8−51 mg in 0.4 mL respective) was added dropwise onto **CZL** powders (1 g) under manual stirring. The powders were standing in ambient conditions for 2 h and then dried in still air at 80 °C for 12 h, followed by air-calcination at 700 °C for 4 h (ramping rate: 2 °C/min).

2.2. Characterization. The X-ray photoelectron spectroscopy (XPS) analysis was performed on an Axis Ultra XPS spectrometer (Kratos, U.K.) with 225 W of Al K$_\alpha$ radiation. The C 1s line at 284.8 eV was used to calibrate the binding energies. The surface concentration of platinum was determined by integrating the areas of Pt 4f, Ce 3d, Zr 3d, and La 3d peaks in the CasaXPS software.

Vis-Raman spectra were acquired by excitation of the sample at 532 nm, using a Raman microscope system (HORIBA JOBIN YVON) in a spectral window from 100 to 800 cm^{-1} with a resolution of 2 cm^{-1}.

The powder X-ray diffraction (XRD) patterns were recorded on a Bruker D8 Advance diffractometer (40 kV, 40 mA) with a scanning rate of 4° min^{-1}, using Cu K$_{\alpha1}$ radiation (λ = 1.5406 Å). The diffraction patterns were collected from 20 to 80° with a step of 0.02°. The 2θ angles were calibrated with a micrometer-scale Alumina disc. The powder sample after grinding was placed inside a quartz sample holder for each test. With the software "LAPOD" of least-squares refinement of cell dimensions of cubic **CZL** from powder data by Cohen's method.[32,33]

The nitrogen adsorption/desorption measurements were performed on an ASAP2020-HD88 analyzer (Micromeritics Co. Ltd.) at 77 K. The measured powders were degassed at 250 °C under vacuum (<100 μmHg) for over 4 h. The BET specific surface areas (S_{BET}) were calculated from data in the relative pressure range between 0.05 and 0.20. The pore diameter (D_p) distribution was calculated from the adsorption branch of the isotherms, based on the BJH method.[34]

The TEM and high-resolution TEM (HRTEM) experiments were carried out on a FEI Tecnai G^2 F20 microscope operating at 200 kV with energy dispersive spectroscopy (EDS) to determine the platinum loadings. All the tested samples were suspended in ethanol, and then a drop of this dispersed suspension was placed on an ultrathin (3−5 nm in thickness) carbon film-coated Cu grid. The as-formed sample grid was dried naturally under ambient conditions before loaded into the TEM sample holder.

The aberration-corrected HAADF-STEM images were carried out on a JEOL ARM200F microscope equipped with probe-forming spherical-aberration corrector. Owing to the relatively high atomic number of cations in the **CZL** support, the contrast of Pt in HAADF images is not clear, particularly for the thick region. Here, to enhance the contrast difference between the Pt and Ce, we set the inner and outer angles of the HAADF detector to be 90 and 370 mrad, respectively, and the convergence angle to be ca. 30 mrad.

The XAFS spectra at Pt L$_3$-edge (E_0 = 11564.0 eV) was performed at BL14W1 beamline[35] of Shanghai Synchrotron Radiation Facility (SSRF) operated at 3.5 GeV under "top-up" mode with a constant current of 260 mA. The XAFS data were recorded under fluorescence mode with a seven-element Ge solid state detector. The energy was calibrated accordingly to the absorption edge of pure Pt foil. Athena and Artemis codes were used to extract the data and fit the profiles. For the X-ray absorption near edge structure (XANES) part, the experimental absorption coefficients as a function of energies $\mu(E)$ were processed by background subtraction and normalization procedures, and reported as "normalized absorption" with E_0 = 11564.0 eV for all **Pt-CZL** samples and Pt foil/PtO$_2$ standard. Based on the normalized XANES profiles, the molar fraction of Pt^{4+}/Pt^0 can be determined by the linear combination fit[36] with the help of various references (Pt foil for Pt^0 and PtO$_2$ for Pt^{4+}). For the extended X-ray absorption fine structure (EXAFS) part, the Fourier transformed (FT) data in R space were analyzed by applying PtO$_2$ and metallic Pt model for Pt−O and Pt−Pt contributions. The passive electron factors, S_0^2, were determined by fitting the experimental data on Pt foils and fixing the coordination number (CN) of Pt−Pt to be 12, and then fixed for further analysis of the measured samples. The parameters describing the electronic properties (e.g., correction to the photoelectron energy origin, E_0) and local structure environment including CN, bond distance (R), and Debye−Waller factor around the absorbing atoms were allowed to vary during the fit process. The fitted ranges for k and R spaces were selected to be k = 3−10 Å^{-1} (**0.5Pt-CZL**), 3−11 Å^{-1} (**1Pt-CZL**), or 3−12 Å^{-1} (**2Pt-CZL**) with R = 1.1−4.0 Å (k^3 weighted). To distinguish the effect of the Debye−Waller factor from coordination number, we set σ^2 to be 0.0030 and 0.0045 Å^2 for all the analyzed Pt−O and Pt−Pt shells, according to the fitted results of Pt foil and PtO$_2$ standards. We also set σ^2 to be 0.0045 Å^2 for all the analyzed Pt−Ce paths, considering that the z number of Ce (58) is close to that of Pt (78), as well as the absence of an appropriate standard for the Pt−Ce shell. To distinguish the effect of correction to the photoelectron energy origin from distance, we set ΔE_0 to be 14.1/13.7, 13.7/13.7, and 11.6/11.3 eV for fresh/used **0.5Pt-CZL**, **1Pt-CZL**, and **2Pt-CZL**, respectively, which were obtained from the linear combination fits on XANES profiles and the fitting results of Pt foil (ΔE_0 = 8.3 ± 1.2 eV) and bulk PtO$_2$ (ΔE_0 = 15.0 ± 0.9 eV) standards.

2.3. Catalytic Tests. The temperature-programmed reduction by hydrogen (H$_2$-TPR) was performed in a Builder PCSA-1000 instrument (Beijing, China) equipped with a thermal conductivity detector (TCD). The fresh catalysts (40−60 mesh, 30 mg) were pretreated in pure O$_2$ at 300 °C for 30 min and cooled to room temperature in the same atmosphere. The reduction process was carried out in a mixture of 5% H$_2$/Ar (30 mL/min) from room-temperature to 750 °C (5 °C min^{-1}).

CO pulse chemisorption measurements were performed on AutoChemII 2920 instrument at low temperature. The sample was heated to 400 °C in a 5%H$_2$/He flow (30 mL/min) holding for 30 min and cooled to the room temperature in the same gas composition. Then, the sample was placed into the isopropanol− liquid nitrogen mixture holding the temperature between 195−198 K in a helium flow. CO pulses were injected at that temperature until the adsorption reached saturation. The concentration of the CO pulse was determined by a thermal conductivity detector (TCD).

The CH$_4$ combustion activities for the **Pt-CZL** samples were evaluated in a plug flow reactor using 50 mg of sieved (40−60 mesh) powders in a gas mixture of 1 vol % CH$_4$, 5 vol % O$_2$, and 94 vol % N$_2$ (from Jinan Deyang Corporation, 99.997% purity) at a flow rate of 41.6 mL/min giving a gas hourly space velocity (GHSV) of ~50,000 mL·g$_{cat}$$^{-1}$·h^{-1}. The catalysts were pretreated in pure O$_2$ at 500 °C for 30 min before reaction. After the catalysts cooled down to room temperature under a flow of pure N$_2$ gas, reactant gases was passed through the reactor. The concentrations of outlet gases were analyzed by an online GC (Ouhua GC 9160), which is equipped with a thermal conductivity detector (TCD) and Porapark Q column. The related stability tests were done in the same conditions at the constant reaction temperature of 600 °C for 10 h with a GHSV of ~100,000 mL·g$_{cat}$$^{-1}$·h^{-1}. CH$_4$ conversion was defined as (CH$_{4,inlet}$ − CH$_{4,outlet}$)/CH$_{4,inlet}$ × 100%, where CH$_{4,inlet}$ and CH$_{4,outlet}$ are the inlet and outlet concentrations of methane, respectively. Rate measurements were made in the separate catalytic tests rather than the "light-off" mode, i.e., the same gas composition, but at specific space velocities to ensure operation in the kinetic regime (<20% conversion of CH$_4$).

To minimize the possible structural changes of used catalysts for the related characterizations (XRD, Raman, XPS, XAFS, TEM/HRTEM, and HAADF-STEM), the platinum-doped ceria−zirconia−lanthana samples after the methane oxidation reaction were quickly transferred to vials filled with N$_2$ gas, and the vials were opened just before the further measurements.

3. RESULTS

3.1. Catalytic Reactivity and Reducibility of Pt-CZL Catalysts. Methane oxidation reaction (CH$_4$ + 2O$_2$ = CO$_2$ + 2H$_2$O) was used to evaluate the catalytic performance of platinum-doped ceria−zirconia−lanthana catalysts. The "light-off" profiles were obtained under a GHSV of 50,000 mL·g^{-1}·h^{-1}, and Figure 1a shows that all the **Pt-CZL** samples exhibited significantly higher methane conversions than the pure **CZL** support in the temperature range of 300−650 °C, indicating the importance of doped platinum to activate the oxidation of methane. Figure 1b displays the results for stability tests obtained under a higher GHSV of 100,000 mL·g^{-1}·h^{-1}. The methane conversions after 10 h reaction at 600 °C keep this sequence: **2Pt-CZL** (76%) > **1Pt-CZL** (70%) > **0.5Pt-CZL** (55%) > **CZL** (38%), well consistent with the loading amount of platinum. Recently, Stakheev et al. reported about 60% methane oxidation at 550 °C under 60,000 mL·g^{-1}·h^{-1} over 0.8 wt % Pt/Al$_2$O$_3$,[37] and Arandiyan et al. observed 90% methane conversion at 600 °C under ~30,000 mL·g^{-1}·h^{-1} over 1.1 wt % Pt/Ce$_{0.6}$Zr$_{0.3}$Y$_{0.1}$O$_2$.[20] Therefore, the reactivity of current **Pt-CZL** samples is comparative
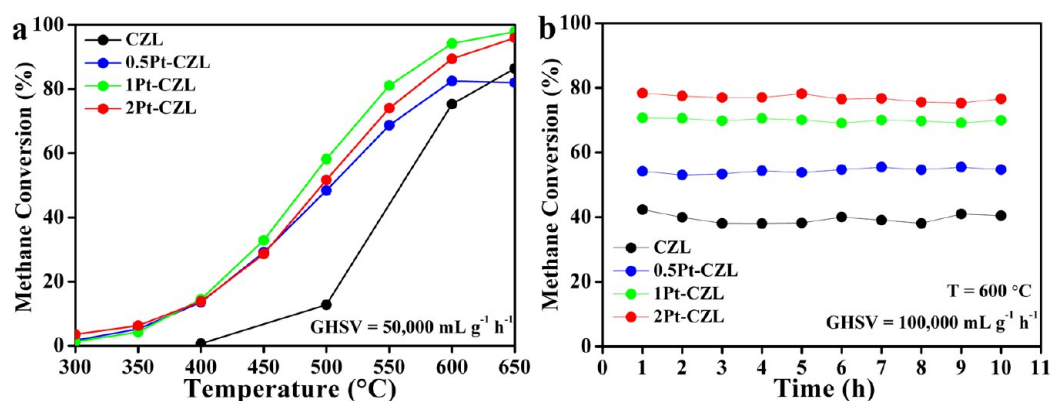
Figure 1. Methane conversion over **Pt-CZL** samples for (a) "light-off" experiments from 300 to 650 °C and (b) stability tests at 600 °C for 10 h.
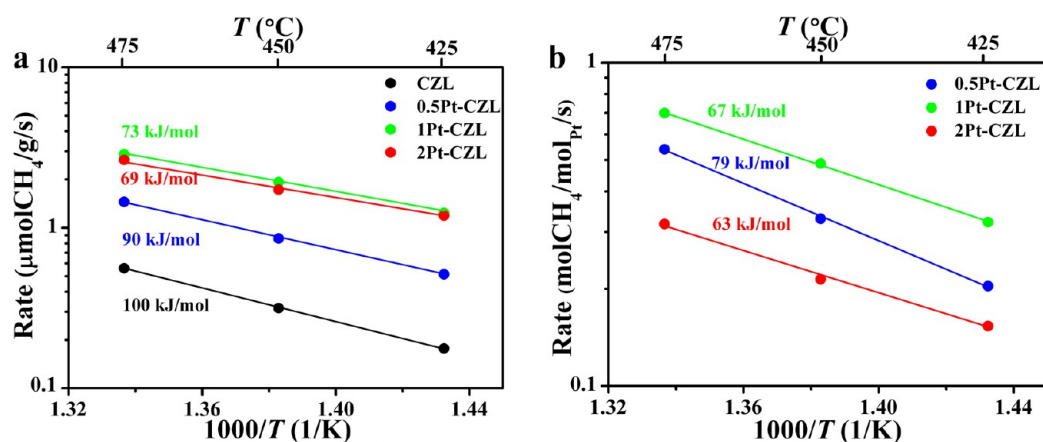

Figure 2. Arrhenius plots for the oxidation of methane over **Pt-CZL** samples: (a) total rates and (b) exclusive rates from Pt contribution.

Table 1. H$_2$-TPR Peak Areas (H_2), Total Rates Normalized by Catalyst Weight (r_w), Exclusive Rates from Pt Contribution Normalized by Platinum Amount (r_{Pt}), Apparent Activation Energies (E_a), and Exclusive Activation Energies from Pt Contribution (E_{Pt}) for the Methane Oxidation Reaction over Pt-CZL/CZL Samples

sample	H_2 (a.u.)	r_w ($\mu mol_{CH4} \cdot g_{cat}^{-1} \cdot s^{-1}$)			r_{Pt} ($mmol_{CH4} \cdot mol_{Pt}^{-1} \cdot s^{-1}$)			E_a (kJ/mol)	E_{Pt} (kJ/mol)
		425 °C	450 °C	475 °C	425 °C	450 °C	475 °C		
CZL	1230	0.18	0.32	0.56				100 ± 1	
0.5Pt-CZL	1430	0.52	0.87	1.47	10.3	16.7	27.4	90 ± 2	79 ± 2
1Pt-CZL	1200	1.24	1.93	2.87	16.1	24.4	35.0	73 ± 1	67 ± 2
2Pt-CZL	1120	1.19	1.73	2.65	7.6	10.6	17.3	69 ± 4	63 ± 4

to these reported supported platinum catalysts, if considering the effect of space velocity in the different catalytic tests. Furthermore, on the basis of stability tests (Figure 1b), no obvious deactivation was detected for **Pt-CZL**, revealing the high catalytic stability of platinum-doped ceria–zirconia–lanthana during the methane oxidation reaction (1 vol % CH$_4$ + 5 vol % O$_2$ + 94 vol % N$_2$, ~100,000 mL·g^{-1}·h^{-1}, 600 °C).

According to the kinetics data of the platinum-doped ceria–zirconia–lanthana samples, we calculated the total reaction rates normalized by catalyst weight (r_w). Figure 2a and Table 1 show that the pure **CZL** support itself did activate the oxidation of methane, but the efficiency (r_w = 0.18–0.56 $\mu mol_{CH4} \cdot g_{cat}^{-1} \cdot s^{-1}$ at 425–475 °C) was relatively lower than the **Pt-CZL** catalysts. When a small amount of platinum was introduced, **0.5Pt-CZL** shows nearly triple numbers of r_w (0.52–1.47 $\mu mol_{CH4} \cdot g_{cat}^{-1} \cdot s^{-1}$ at 425–475 °C) compared to **CZL**, due to the significant promotion effect of active Pt species. As the concentration of Pt increases, the r_w values of **1Pt-CZL** (1.24–2.87 $\mu mol_{CH4} \cdot g_{cat}^{-1} \cdot s^{-1}$

at 425–475 °C) and **2Pt-CZL** (1.19–2.65 $\mu mol_{CH4} \cdot g_{cat}^{-1} \cdot s^{-1}$ at 425–475 °C) are almost identical (Figure 2a and Table 1), giving a hint that the efficiency normalized by catalyst weight reaches the maximum at 1 at. % Pt. The apparent activation energy (E_a) numbers were also calculated from the Arrhenius plots at the low methane conversion range (<20%), corresponding to the above temperature range (425–475 °C) (see Table S1 for details). Table 1 shows that the E_a of pure oxide support is as high as 100 kJ mol^{-1}, revealing that **CZL** may need high temperature to activate (Figure 1a). Recently, Lee et al. determined that the E_a of pure ceria is 115.6 kJ mol^{-1} for the oxidation of methane,[38] which is very close to ours. Similar to the trend of reaction rates, the introduction of a small platinum sample (**0.5Pt-CZL**) gives a lower E_a (90 kJ mol^{-1}) than **CZL**, and **1Pt-CZL** and **2Pt-CZL** have nearly constant activation energies as low as ~70 kJ mol^{-1} (see Table 1). Again, Lee et al. reported the Pt@CeO$_2$ catalysts with different Pt sizes show the E_a of 65–82 kJ mol^{-1},[38] well consistent with our experimental results.

To distinguish the platinum fraction from the total reaction rates or apparent activation energies, we subtracted the contribution of **CZL** support and normalized the residual rates by Pt amount to obtain the exclusive rates from Pt contribution (r_{Pt}). It can be seen from Figure 2b and Table 1 that the catalytic reactivity on methane oxidation follows this order: **1Pt-CZL > 0.5Pt-CZL > 2Pt-CZL**. Obviously, 1 at. % Pt shows the highest platinum efficiency with the r_{Pt} values of 16.1−35.0 mmol$_{CH4}$· mol$_{Pt}^{-1}$·s^{-1} at 425−475 °C. Recently, Arandiyan et al. reported 1.1 wt % Pt/Ce$_{0.6}$Zr$_{0.3}$Y$_{0.1}$O$_2$ catalysts showing a reaction rate of ∼7 mmol$_{CH4}$·mol$_{Pt}^{-1}$·s^{-1} at 400 °C.[20] Thus, our present platinum-doped ceria−zirconia−lanthana catalysts have almost equal or even higher reactivity on the oxidation of methane than those in the literature (see Table 2 for details). Besides, the exclusive activation energies from Pt contribution (E_{Pt}), which were calculated according to the r_{Pt} values, have been included (Figure 2b, Table 1). The calculated E_{Pt} numbers are within the range of 70 ± 10 kJ mol^{-1} for all the **Pt-CZL** samples and lower than the related E_a values, indicating the low-temperature activity is more dependent upon the efficiency of platinum.

Hydrogen temperature-programmed reduction (H$_2$-TPR) was applied to investigate the reducibility of platinum-doped ceria−zirconia−lanthana catalysts. Figure S1a displays that for the pure **CZL** support, the main peak is located at 590 °C, due to the reduction of Ce^{4+}→ Ce^{3+} in nanosized ceria.[39] The introduction of platinum led to a significant decrease of this reduction temperature to around 200 °C, indicating a pronounced Pt−O−Ce interaction.[40] The reduction peak of **2Pt-CZL** (186 °C) is obviously at lower temperature than those of **0.5Pt-CZL** (240 °C) and **1Pt-CZL** (236 °C), giving a hint of the presence of a weaker metal−support interaction in the high-concentration platinum sample.[41] Figure S1b shows that the peak areas of H$_2$-TPR profiles, which are proportional to the hydrogen consumption values or the surface oxygen numbers, are very close between the pure **CZL** support and the **Pt-CZL** catalysts. So, the introduction of a small amount (0.5−2 at. %) of platinum can fully activate the surface oxygen species, which are related to the ceria−zirconia−lanthana support, at low temperature, below 300 °C.

3.2. Structural and Textural Properties on Pt-CZL Catalysts. The bulk concentrations of platinum (Pt$_{bulk}$) were determined by EDS. Table 3 shows that the Pt$_{bulk}$ values are 0.5, 1.0, and 1.7 at. % for **0.5Pt-CZL**, **1Pt-CZL**, and **2Pt-CZL**, respectively, close to these designed numbers. It gives a hint of the successful impregnation process in our synthesis. The surface concentrations of platinum (Pt$_{surf.}$) were decided by X-ray photoelectron spectroscopy (XPS). Table 3 shows that the Pt$_{surf.}$ values are 1.1, 1.8, and 2.8 at. % for **0.5Pt-CZL**, **1Pt-CZL**, and **2Pt-CZL**, respectively, distinctly higher than those of Pt$_{bulk}$. This can be explained because the escape depth of photoemitted electrons is short (normally a few nanometers) and the inlet X-ray cannot fully penetrate the **CZL** matrix in experiments. Furthermore, Table 3 also displays that the Pt$_{surf.}$ numbers after the oxidation of methane are 1.1, 1.8, and 2.7 at. % for

Table 2. Comparison of the Activities over the Representative Platinum Catalysts for the Methane Oxidation Reaction

	temp (°C)	gas feed composition	reaction rate by catalyst weight (μmol$_{CH4}$·g$_{cat}^{-1}$·s^{-1})	reaction rate by Pt amount (mmol$_{CH4}$·mol$_{Pt}^{-1}$·s^{-1})	apparent activation energy (kJ/mol)	ref
Inert supports						
1.9 wt % Pt/Al$_2$O$_3$	380	2%CH$_4$/5%O$_2$/He	0.034	0.35	90	13
4.1 wt % Pt/Al$_2$O$_3$	300	1%CH$_4$/16%O$_2$/Ar	0.083	0.40		54
Reducible oxide supports						
1.1 wt % Pt/CZY	300	2%CH$_4$/20%O$_2$/N$_2$	0.11	1.86	66	20
	350		0.21	3.68		
	400		0.39	6.98		
Our results						
1 at. % Pt/CZL	425	1%CH$_4$/5%O$_2$/N$_2$	1.24	16.1	73	
	450		1.93	24.4		
	475		2.87	35.0		
	300		0.08[a]	1.2[a]		
	350		0.27[a]	4.1[a]		
	400		0.77[a]	11.7[a]		

[a]Calculated values on the basis of extended points in Arrhenius plots.

Table 3. Bulk and Surface Pt Concentration (Pt$_{bulk}$ and Pt$_{surf.}$), BET Specific Surface Areas (S_{BET}), BJH Pore Volume (V_p), Position for F_{2g} Peak in Raman, Lattice Constants (a) of Pt-CZL/CZL Samples, Averaged Grain Sizes (D_{XRD}) and Particle Sizes (D_{TEM}) of CZL Support, and Average Pt Cluster Sizes (D_{Pt}) for Pt-CZL Samples

sample	Pt$_{bulk}$ (at. %)[a]	Pt$_{surf.}$ (at. %)[b]	S_{BET} (m^2/g)[c]	V_p (cm^3/g)[c]	F_{2g} (cm^{-1})[d]	a (Å)[e]	D_{XRD} (nm)[f]	D_{TEM} (nm)[g]	D_{Pt} (nm)[i]
CZL			56	0.112	476	5.3536(1)	6.6	7.1 ± 1.5	
					465[f]	5.3599(1)[h]	6.4[h]	6.9 ± 1.0[h]	
0.5Pt-CZL	0.5	1.1	57	0.115	473	5.3532(2)	6.7	7.4 ± 1.2	2.4 ± 0.6
		1.1[h]			461[f]	5.3540(1)[h]	6.2[h]	7.1 ± 1.0[h]	
1Pt-CZL	1.0	1.8	53	0.113	471	5.3525(1)	6.5	7.2 ± 1.2	1.8 ± 0.4
		1.8[h]			458[f]	5.3535(1)[h]	6.8[h]	6.9 ± 1.2[h]	
2Pt-CZL	1.7	2.8	55	0.110	466	5.3548(3)	6.6	7.4 ± 1.3	<1
		2.7[h]			452[f]	5.3565(1)[h]	6.3[h]	7.1 ± 1.1[h]	

[a]Calculated by EDS. [b]Calculated by XPS. [c]From N$_2$ adsorption/desorption experiments. [d]Determined by Raman spectra. [e]Calculated from the XRD patterns by least-squares estimation. [f]Calculated from the XRD patterns by Scherrer equation. [g]Statistic data on the basis of TEM images. [h]For used samples after methane oxidation reaction. [i]Statistic data on the basis of aberration-corrected HAADF-STEM images.

0.5Pt-CZL, **1Pt-CZL**, and **2Pt-CZL**, respectively, indicating good stability of platinum dispersion during reaction (600 °C, 10 h, 1 vol % CH$_4$ + 5 vol % O$_2$ + 94 vo % N$_2$, 600 °C).

The nitrogen adsorption/desorption experiments were carried out to investigate the textural properties of platinum-doped ceria−zirconia−lanthana catalysts. Representative nitrogen adsorption/desorption isotherms are shown in Figure S2a. All the curves, whether for **Pt-CZL** catalysts or pure **CZL** support, can be attributed to type IV, characteristic of capillary condensation taking place in mesopores.[42] The hysteresis loops in the P/P_0 range of 0.6−0.9 associated with this isotherm are classified to type H1, quite typical of porous materials consisting of agglomerates, or compacts of approximately uniform spheres in a fairly regular array.[42] Table 3 shows that the BET specific surface areas and BJH pore volumes of as-calcined samples are almost identical between **Pt-CZL** (53−57 m^2/g, 0.110−0.115 cm^3/g) and **CZL** (56 m^2/g, 0.112 cm^3/g). Here, we noticed that the typical pore volume determined by nitrogen adsorption/desorption experiments (∼0.1 cm^3/g) is much smaller than the amount of water we used during impregnation (0.4 mL/g) since the **CZL** support has extra interaction to the polar solvent (H$_2$O) than to the nonpolar gas molecule (N$_2$). Figure S2b shows that all the **Pt-CZL** samples have narrower distributions on pore size than **CZL**, giving a hint of the interaction between platinum metal and oxide support. It indicates that the deposition of platinum actually did not affect the major textural properties of ceria−zirconia−lanthana in our synthesis.

The XRD tests were performed to determine the crystal structure of platinum-doped ceria−zirconia−lanthana catalysts. The XRD patterns in Figure 3a identify that all the fresh **Pt-CZL**/**CZL** samples are of a fluorite face-centered-cubic (*fcc*) CeO$_2$ phase (JCPDS card no.: 34−394) with lattice constant a of 5.3525−5.3548 Å (see Table 3) after the impregnation step and the sequential air calcination at 700 °C. The average grain sizes estimated by Scherrer equation for **Pt-CZL**/**CZL** (6.5−6.7 nm) are in good agreement with the averaged pore sizes obtained by nitrogen adsorption/desorption and almost identical (see Table 3) since these supports were initially sintered at the higher temperature of 800 °C. Figure 3a also confirms that no Pt/PtO$_2$ phases were detected for **0.5Pt-CZL**, revealing that the deposited platinum species are of small size (less than ca. 2 nm) over the **CZL** support. For **1Pt-CZL**, a very tiny band of Pt (*fcc*, JCPDS card no.: 4−802) around 40° was found in XRD, indicating the possible presence of small-size platinum metals. However, for **2Pt-CZL**, narrow diffraction peaks at 39.7, 46.2, 67.4, and 81.2° were clearly observed, which can be assigned to metallic Pt phase (a = 3.9230(1) Å).

All the above experimental data demonstrate a monotonous trend for the decrease on dispersion of platinum species, or the increase on the formation of metallic Pt crystals, with the Pt concentration. Previously, Lee et al. synthesized 0.75 wt % Pt−Ce/C samples with NaBH$_4$ reduction, which shows the *fcc* Pt phase after calcination at 150 °C for 2 h.[43] Later on, Kamiuchi et al. found that after calcinations at 800 °C for 3 h, 1.0 wt % Pt/CeZrO$_x$ showed obvious diffraction peaks of Pt metal.[44] Therefore, the current impregnation method utilized in this work was powerful to maintain the small-size platinum species up to ca. 1 at. % Pt, which is due to the high thermal stability of single-phase **CZL** support.[27] Furthermore, Figure 3b displays that the **Pt-CZL** samples after methane oxidation reaction (the stability tests at 600 °C for 10 h) maintained exactly the same crystal structure. It demonstrates the high reaction stability of **Pt-CZL** samples during the methane oxidation reaction.

Visible Raman excited by 532 nm laser was applied to finely determine the structure of platinum-doped ceria−zirconia−lanthana samples. Figure 4a distinctly exhibits a strong absorption centered at 466−476 cm^{-1}, corresponding to the triply degenerate F_{2g} mode of fluorite CeO$_2$.[45] Table 3 shows that the position of the F_{2g} Raman peak for **Pt-CZL** is inversely proportional to the Pt loading amount, from 476 (**CZL**) to 466 cm^{-1} (**2Pt-CZL**). It can be explained by the formation of more oxygen vacancies with the addition of more platinum species.[46] Previously, Lee et al. has confirmed that the F_{2g} Raman peak shifts in CeO$_{2-\delta}$ and Au/CeO$_{2-\delta}$ nanoparticles decrease during the oxidation of CO because of the increase of oxygen vacancies.[47] Figure 4b shows that after the oxidation of methane, the F_{2g} peak position of **CZL** or **Pt-CZL** shifted to lower wavenumber (465−452 cm^{-1}), compared to the related fresh counterpart (476−466 cm^{-1}).

The TEM and HRTEM characterizations were used to determine the morphology, size, and shape of platinum-doped ceria−zirconia−lanthana catalysts under a microdomain view. The TEM images in Figure 5a,c,e display that the fresh **Pt-CZL** catalysts were composed by polyhedron-like nanocrystals. Table 3 shows that the averaged particle size estimated from the statistical data is 7.1−7.4 nm for all the measured samples, in good agreement with XRD results (6.5−6.7 nm). The HRTEM images in Figure 5b,d,f exhibit that the interplanar distance for lattice fringes of nanocrystals in fresh **Pt-CZL** is 0.31−0.32 nm, attributed to the (111) planes for doped ceria. Pt is invisible in both TEM and HRTEM images of **Pt-CZL** samples, except for **2Pt-CZL**, showing some very large (50−100 nm) Pt particles, which is well consistent with the presence of sharp peaks in XRD.
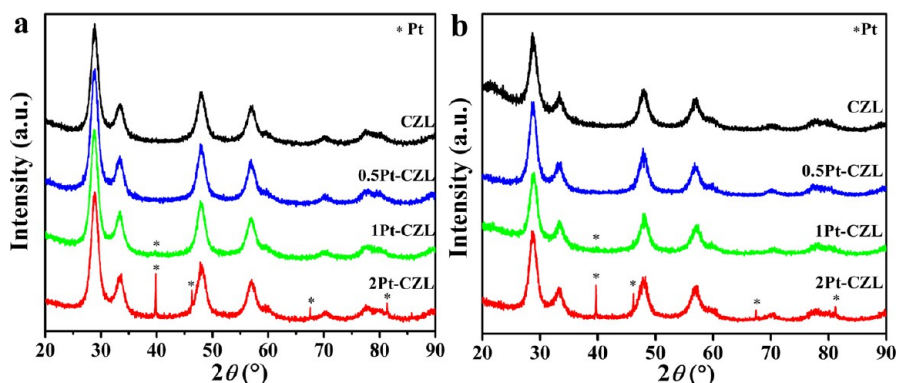

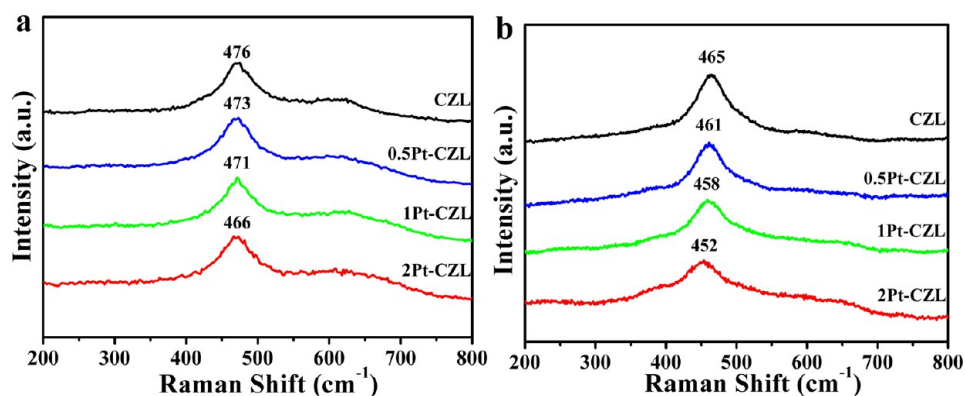**Figure 3.** XRD patterns of **Pt-CZL** samples: (a) fresh and (b) used.

Figure 4. Raman spectra of **Pt-CZL** samples: (a) fresh and (b) used.
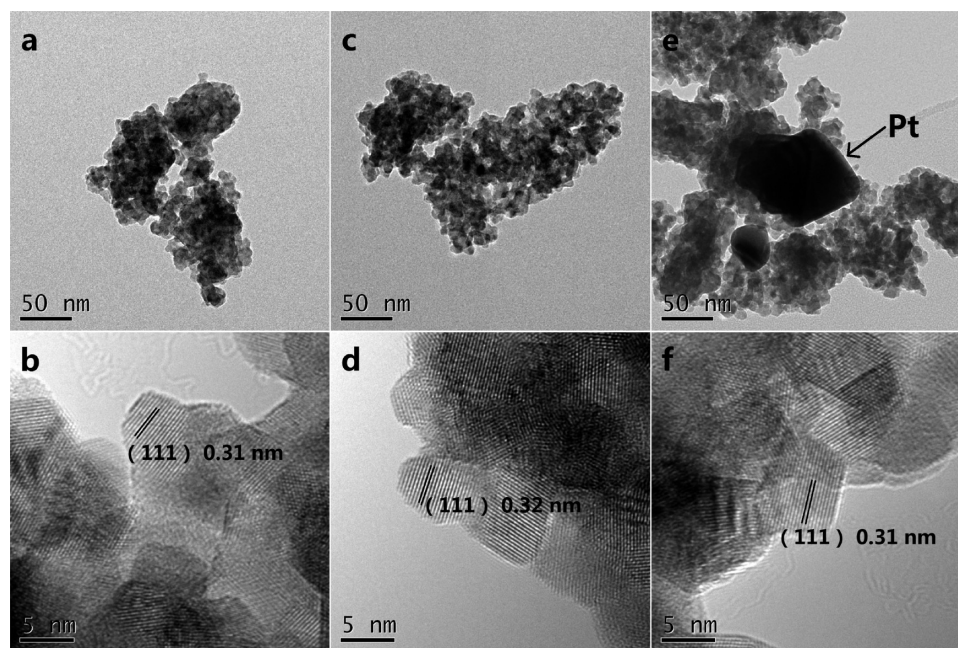

Figure 5. TEM (a,c,e) and HRTEM (b,d,f) images of fresh **Pt-CZL** samples: (a,b) **0.5Pt-CZL**; (c,d) **1Pt-CZL**; (e,f) **2Pt-CZL**.

Figure S3 shows the TEM and HRTEM images of the used **Pt-CZL** catalysts after oxidation of methane at 600 °C for 10 h. The polyhedron shape (Figures S3a,c,e) and small size (6.7−7.1 nm, see Table 3) of nanocrystals were maintained, as well as the identification of doped ceria from the interplanar distance (0.32 nm, see Figures S3b,d,f). Again, only **2Pt-CZL** contains large-size Pt particles in TEM (Figure S3e). Thus, the structure of **Pt-CZL** nanocrystals displays very high stability against the methane oxidation process. Recently, Vita et al. reported that after undergoing methane oxysteam, reforming between 500−800 °C for 60 h, the average size of Pt nanoparticles determined by TEM was very stable at 5.8−5.9 nm.[48]

3.3. Electronic and Local Coordination Structure of Platinum in Pt-CZL Catalysts. To observe the size and dispersion of platinum species, we employed the aberration-corrected HAADF-STEM to characterize the platinum-doped ceria−zirconia−lanthana catalysts. Typically, Figure 6 exhibits the HAADF-STEM images of fresh **Pt-CZL** samples under different magnifications. Figure 6a depicts the ultrafine clusters with size of 2.4 ± 0.6 nm and narrow size-distribution (Figure S4a) over the oxide matrix for **0.5Pt-CZL**, which are actually non-crystalline and composed by platinum atoms according to the

contrast picture in Figure 6b. Recently, Ke et al. synthesized subnanometric PtO_x clusters supported on the CeO_2 nanowires and found that the size of platinum clusters was ca. 0.5 nm by HAADF-STEM.[40] As the Pt amount increases, **1Pt-CZL** shows the existence of ultrafine clusters (Figure 6c) with an average size of 1.8 ± 0.4 nm (Figure S4b). Besides, ca. 4 nm Pt metallic crystals with clear lattice fringe also exist in the fresh **1Pt-CZL** samples (Figure S5).

However, for **2Pt-CZL**, the HAADF-STEM results confirmed the presence of extremely fine platinum clusters less than 1 nm (Figure 6e and black arrows in Figure 6f). Therefore, by the aid of aberration-corrected HAADF-STEM technique, we can verify that the sizes of ultrafine clusters show the sequence **0.5Pt-CZL** > **1Pt-CZL** ≫ **2Pt-CZL**. Here, we cannot attribute these ultrafine clusters to either metallic Pt or ionic platinum oxide phase since lattice oxygen is unable to be distinguished from the surrounding circumstances in HAADF-STEM. Besides, the white circles in Figure 6b,d,f clearly display the individual platinum atoms for **0.5Pt-CZL**, **1Pt-CZL**, and **2Pt-CZL**, respectively. Here, the creation of Pt single atoms in all the fresh samples after air calcination as high as 700 °C has been rarely reported.[49] Also, for **2Pt-CZL**, the presence of both large-size Pt particles
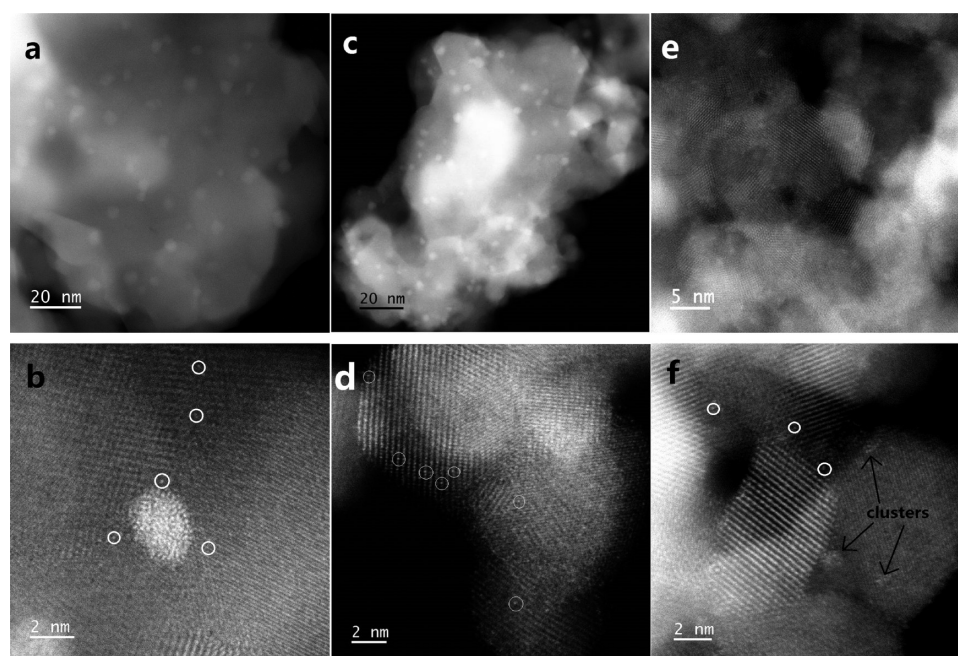
Figure 6. Aberration-corrected HAADF-STEM images of fresh **Pt-CZL** samples: (a,b) **0.5Pt-CZL**; (c,d) **1Pt-CZL**; (e,f) **2Pt-CZL**. White circles and black arrows present single atoms and clusters, respectively.

(Figure 5e) and ultrafine platinum clusters as well as single atoms (Figures 6e,f) reveal that the particle size distribution of platinum in this sample is strictly bimodal.

The EXAFS part with the profile fitting in R space was carried out to determine the short-range local coordination structure including distances (R) and coordination number (CN) around the studied platinum atoms. The fitted ranges for k spaces were selected to be $k = 3-10$ Å^{-1} (**0.5Pt-CZL**), $3-11$ Å^{-1} (**1Pt-CZL**), and $3-12$ Å^{-1} (**2Pt-CZL**), based on experimental data (Figure S6). On the basis of EXAFS fitting results (Figure 7c,d and Table 4), we found nearly the same results between fresh and used catalysts and obtained the following conclusions.

(1) A strong peak at ca. 2 Å with CN of 2.8−5.5 was identified for the first Pt−O shell, which is attributed by the scattering between platinum center and the surrounding oxygen atoms in multiple possibilities of ionic single atoms (Pt$^{\delta+}$−O), ultrafine clusters (Pt$_x$O$_y$), and/or crystallized particle (PtO$_2$) forms. The fitted R values are very close to those of ceria-supported platinum oxide clusters (2.02 Å).[49] Besides, Figure 8a shows that as the concentration of Pt increases, the CN of the first Pt−O shell monotonously decreases, especially for **2Pt-CZL** ($CN = 2.8-3.0$). This can be explained by the formation of a high fraction of metallic Pt particles, which has been confirmed by XRD.

(2) Weak Pt−Pt shell at $R = 3.21-3.23$ Å ($CN = 1.3-3.6$) can be verified, which originates from the Pt−O−Pt structure in Pt$_x$O$_y$ species.[50] Meanwhile, Figure 8b shows that the CN values of this Pt−Pt shell keep the sequence **1Pt-CZL** (2.8−3.6) > **0.5Pt-CZL** (2.3−2.4) > **2Pt-CZL** (1.3−1.6), corresponding to the order for molar fraction of Pt$_x$O$_y$ clusters in each sample. Here, this trend deduced by EXAFS is different from that on cluster size determined by HAADF-STEM (**0.5Pt-CZL** > **1Pt-CZL** ≫ **2Pt-CZL**). It is reasonable since XAFS gives the average signals of all the platinum components and more so focuses on the molar fraction of different species; while HAADF-STEM dominantly provides the direction observations on the size of an individual Pt$_x$O$_y$ cluster.

(3) Much weaker Pt−Ce shell at $R = 3.37-3.45$ Å ($CN = 1.0-1.9$) can be determined by the EXAFS fitting. The origin of this shell should be caused by the metal−support interaction,[51] i.e., **CZL** support is bound to ionic platinum single atoms, ultrafine Pt$_x$O$_y$ clusters, or metallic Pt particles to form Pt−O−Ce interfaces. Figure 8c shows that slightly stronger Pt−O−Ce interaction can be identified for the low-concentration platinum catalysts compared to that for the high-concentration platinum sample (**0.5Pt-CZL** ≈ **1Pt-CZL** > **2Pt-CZL**). This is also consistent with the results of CN of the first Pt−O shell (Figure 8a).

(4) Pt−Pt metallic bond (first shell, $R = 2.78-2.83$; second shell, $R = 3.94$) was determined for **1Pt-CZL** and **2Pt-CZL** with CN values of the first shell equal to 1.5−1.6 and 5.6−5.7, respectively, indicating a greater fraction of the metallic Pt component with an increased platinum amount, from 1 to 2 at. % (Figure 8d). However, no Pt−Pt contribution can be identified for **0.5Pt-CZL**, confirming the absence of crystallized Pt particles for the low-concentration platinum. However, the small CN values of Pt−Pt correspond to the minor fraction of metallic Pt component in **1Pt-CZL**, and thus, the absence of Pt−Pt phase in **0.5Pt-CZL** does not behave as the larger CN values of Pt−Ce. All the above results are in good agreement with the XRD (Figure 3) and TEM (Figure 5 and S3) data.

Therefore, with the help of EXAFS data analysis, we can reliably obtain the local structures of different platinum species including ionic Pt$^{\delta+}$−O single atoms, ultrafine Pt$_x$O$_y$ clusters, and metallic Pt particles (see Figure 8e for model scheme).

4. DISCUSSION

Small-size platinum species (single atoms, ultrafine clusters, and nanoparticles) supported on reducible metal oxides have been widely investigated because of their unique catalytic properties in diverse reactions.[20,28,38,40] In this work, we used thermally stable ceria−zirconia−lanthana (Ce$_{0.5}$Zr$_{0.42}$La$_{0.08}$O$_x$) as an active oxide support to deposit platinum with different loading amounts from 0.5 to 2 at. % via incipient wetness impregnation. The as-obtained
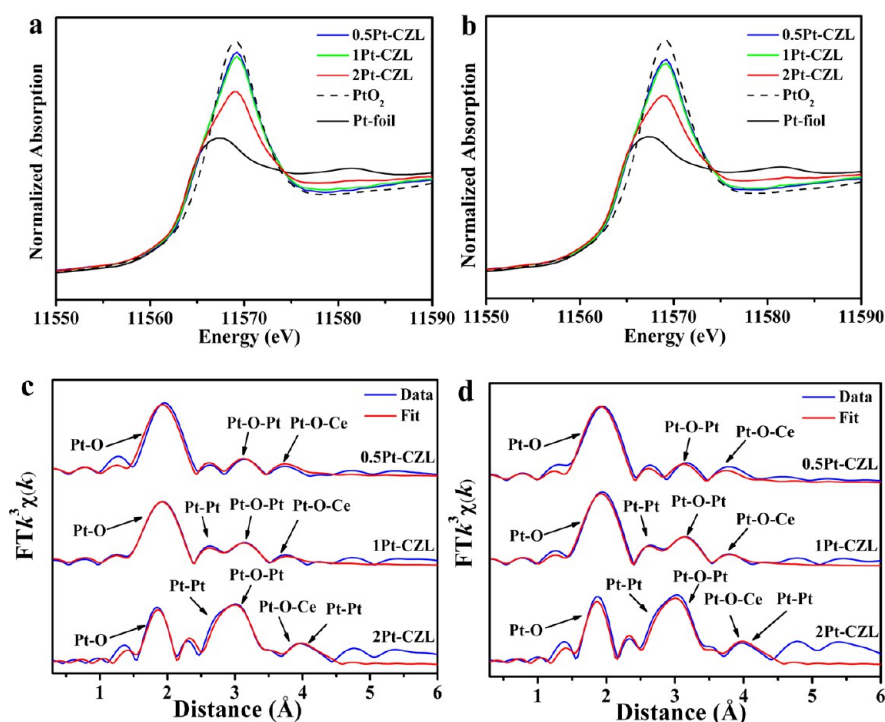
Figure 7. Pt L$_3$-edge XANES profiles (a,b) and EXAFS fitting results in R space (c,d) of **Pt-CZL** samples: (a,c) fresh and (b, d) used.

Table 4. Oxidation State of Platinum (δ) and Pt L$_3$-Edge EXAFS Fitting Results (R, Distance; CN, Coordination Number; σ^2, Debye−Waller Factor[a]; ΔE_0, Inner Potential Correction [b]) of Pt-CZL Samples

		Pt−O		Pt−Pt (metallic)		Pt−Pt (Pt−O−Pt)		Pt−Ce (Pt−O−Ce)	
sample	δ	R (Å)	CN	R (Å)	CN	R (Å)	CN	R (Å)	CN
0.5Pt-CZL (fresh)	3.5	2.00 ± 0.01	5.5 ± 0.3			3.23 ± 0.02	2.4 ± 0.9	3.45 ± 0.03	1.7 ± 0.7
0.5Pt-CZL (used)	3.2	1.99 ± 0.01	5.2 ± 0.3			3.23 ± 0.02	2.3 ± 0.8	3.45 ± 0.03	1.4 ± 0.6
1Pt-CZL (fresh)	3.2	1.99 ± 0.01	4.8 ± 0.3	2.82 ± 0.03	1.5 ± 0.6	3.21 ± 0.01	2.8 ± 0.9	3.44 ± 0.02	1.6 ± 0.5
1Pt-CZL (used)	3.2	2.00 ± 0.01	4.8 ± 0.2	2.83 ± 0.02	1.6 ± 0.4	3.21 ± 0.01	3.6 ± 0.6	3.44 ± 0.02	1.9 ± 0.4
2Pt-CZL (fresh)	2.0	1.98 ± 0.01	3.0 ± 0.3	2.78 ± 0.01	5.7 ± 0.5	3.21 ± 0.02	1.3 ± 1.1	3.37 ± 0.04	1.0 ± 0.7
				3.94 ± 0.01	3.4 ± 0.5				
2Pt-CZL (used)	1.8	1.99 ± 0.01	2.8 ± 0.2	2.79 ± 0.01	5.6 ± 0.6	3.21 ± 0.02	1.6 ± 1.1	3.37 ± 0.04	1.1 ± 0.7
				3.94 ± 0.01	2.8 ± 0.6				

[a]σ^2 = 0.0030, 0.0045, and 0.0045 Å^2 for all the analyzed Pt−O, Pt−Ce, and Pt−Pt shells, respectively; [b]ΔE_0 = 14.1/13.7, 13.7/13.7, and 11.6/11.3 eV for fresh/used **0.5Pt-CZL**, **1Pt-CZL**, and **2Pt-CZL**, respectively, which were obtained from the linear combination fits on XANES profiles and the fitting results of Pt foil (ΔE_0 = 8.3 ± 1.2 eV) and PtO$_2$ (ΔE_0 = 15.0 ± 0.9 eV) standards.

samples showed excellent catalytic performance on the methane oxidation reaction with a high total rate of 1.93 μmol$_{CH4}\cdot$g$_{cat}^{-1}\cdot$s^{-1} and a high Pt-exclusive rate of 24.4 mmol$_{CH4}\cdot$mol$_{Pt}^{-1}\cdot$s^{-1} at 450 °C. Besides, there is a maximal Pt efficiency at ca. 1 at. % Pt (**1Pt-CZL** > **0.5Pt-CZL** > **2Pt-CZL**, see Table 1) based on the exclusive reaction rates by Pt contribution and normalized by Pt amount. Therefore, our platinum-doped ceria−zirconia−lanthana samples are appropriate to be investigated for the structure−activity relationship of the oxidation of methane.

Due to the existence of not only the metallic (Pt^0) and ionic (Pt$^{\delta+}$) components, but also the atoms, clusters, and particles, to distinguish the effects of these components is the highest priority for us to investigate the structure−activity relationship of platinum-doped ceria−zirconia−lanthana catalysts. The aberration-corrected HAADF-STEM technique is important to confirm the presence of the above platinum species from the direct observation (see Figure 6). However, the XAFS measurements, especially the profile fittings on EXAFS spectra, are also indispensable to provide the quantitative results on the

molar fraction of each component (ionic Pt$^{\delta+}$−O single atoms, ultrafine Pt$_x$O$_y$ clusters, and metallic Pt particles) within one investigated sample.

To obtain the molar fraction of different platinum species, first of all, the coordination numbers of the fitted shells (Pt−O, Pt−Pt, and Pt−O−Pt in Table 4) are averaged by the two EXAFS spectra for fresh and used catalysts to improve the fit accuracy (see Table 5). Here, CN of metallic Pt−Pt shell around 2.8 Å is solely determined by the fraction of particles; while CN of Pt−O−Pt at ca. 3.2 Å is independently decided by the fraction of clusters. However, CN of Pt−O at about 2.0 Å includes both contributions from atoms and clusters, and this value subtracting CN of Pt−O−Pt is related to atoms only. We should be careful that these adjusted CN values for atoms/clusters/particles should be normalized by dividing the perfect structural model (ionic atoms and clusters: 8 in PtO$_2$) or practical structural model:[52] 10 for ca. 4 nm Pt particles in **1Pt-CZL** or 12 for 50−100 nm Pt particles in **2Pt-CZL**) before comparison. Here, we obtained the size of the metallic platinum component in
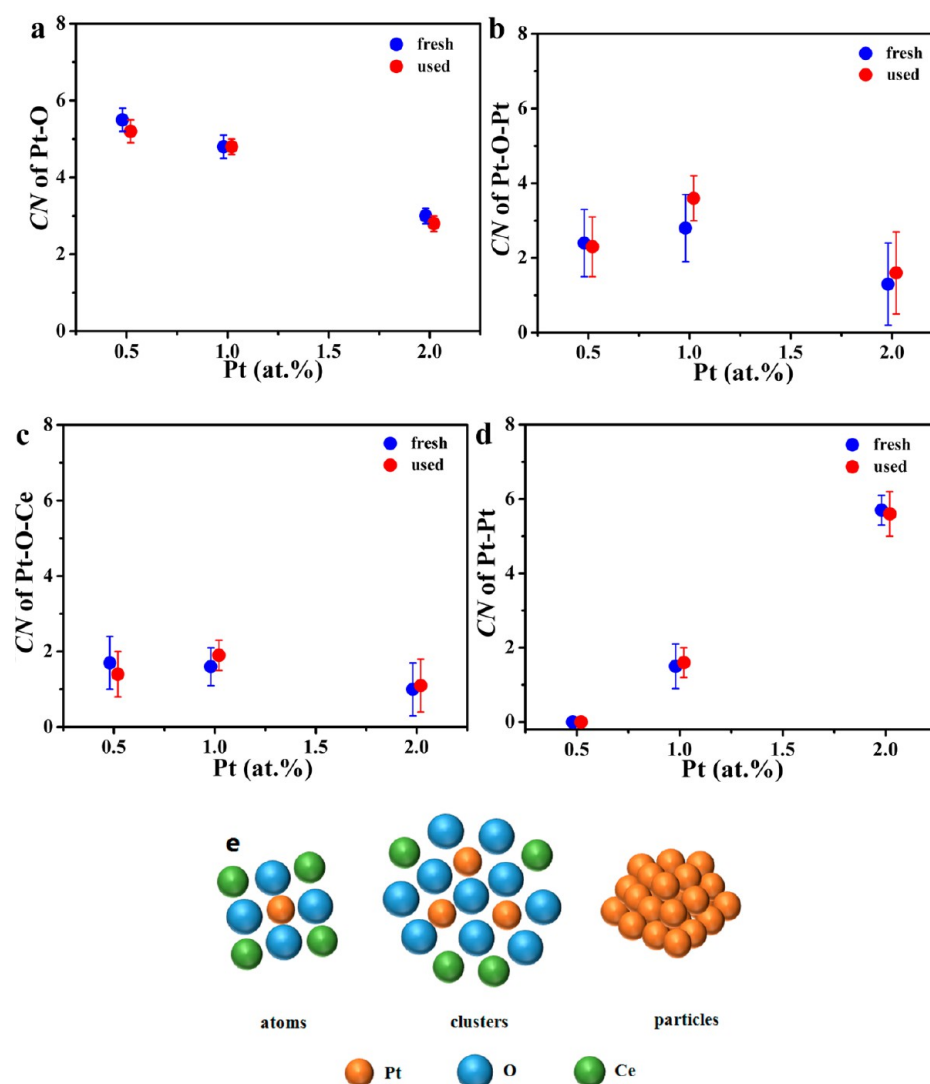
Figure 8. Coordination numbers by EXAFS fitting as a function of platinum concentrations for **Pt-CZL** samples: (a) Pt−O; (b) Pt−O−Pt; (c) Pt−O−Ce; and (d) metallic Pt−Pt. (e) Schematic demonstration on ionic platinum single atoms, ultrafine platinum oxide clusters, and metallic Pt particles.

Table 5. Averaged CN of Pt−O/Pt-Pt/Pt−O−Pt, Molar Fraction of Atom/Cluster/Particle, Calculated Pt Dispersions (d), and Turnover Frequency (TOF) Values for Pt-CZL Samples

	CN							TOF (s⁻¹)		
sample	Pt−O	Pt−Pt	Pt−O−Pt	atom (%)	cluster (%)	particle (%)	d (%)	425 °C	450 °C	475 °C
0.5Pt-CZL	5.4 ± 0.3		2.4 ± 0.9	56 ± 8	44 ± 15	0	74 ± 9	0.014	0.023	0.037
1Pt-CZL	4.8 ± 0.3	1.6 ± 0.7	3.2 ± 0.9	26 ± 6	53 ± 13	21 ± 6	55 ± 9	0.029	0.044	0.064
2Pt-CZL	2.9 ± 0.2	5.7 ± 0.6	1.5 ± 0.7	22 ± 5	22 ± 7	57 ± 6	44 ± 12	0.017	0.024	0.039

1Pt-CZL (ca. 4 nm) and **2Pt-CZL** (50−100 nm) directly from the corresponding experimental data by aberration-corrected HAADF-STEM (Figure S5) and TEM (Figures 5e and S3e), respectively. Therefore, the molar fraction of each platinum species can be finally obtained (**0.5Pt-CZL**: equal atoms and clusters, no particles; **1Pt-CZL**, major clusters plus atoms and particles; **2Pt-CZL**, major particles plus atoms and clusters; see Table 5).

The ceria-based support contains rich oxygen vacancies, which severely affect the chemisorption measurements for the titration of exposed Pt species. So, we estimated the dispersion of platinum by considering both sizes and molar fractions of all the platinum species in each catalyst. For an individual species, atom

reaches 100% of surface Pt; cluster and particle roughly lead to $1/D \times 100\%$ (D: averaged size of each platinum species) of exposed sites. Therefore, we have obtained the dispersion of platinum as 74%, 55%, and 44% for **0.5Pt-CZL**, **1Pt-CZL**, and **2Pt-CZL**, respectively (see Table 5). Obviously, more surface platinum is created with the increasing Pt doping amount. Pt dispersion was also determined by CO pulse chemisorption measurements at low temperature[53] (Table S2). The determined Pt dispersions (36%, 39%, and 23% for **0.5Pt-CZL**, **1Pt-CZL**, and **2Pt-CZL**, respectively) are much lower than those calculated from the EXAFS fitting results. To run CO pulse chemisorption, the transformation from ionic Pt$^{\delta+}$ to metallic Pt^0 component is required and completed by the pre-reduction step. Accompanied

by such H_2-reduction, the presence of these single atoms or ultrafine clusters could be converted to metallic Pt particles (see the XRD patterns in Figure S7 for details). Therefore, in this work, we only calculated the Pt dispersion on the basis of the EXAFS fittings.

Turnover frequency (TOF) is crucial to evaluate the efficiency of active metal and bypass the inside spectators in catalysis. We have obtained the exclusive rates from Pt contribution normalized by platinum amount (unit: $mmol_{CH4}\cdot mol_{Pt}^{-1}\cdot s^{-1}$) in Table 1. Distinctly, **1Pt-CZL** behaves with the highest TOF at various reaction temperatures from 425 to 475 °C; while **0.5Pt-CZL** and **2Pt-CZL** show almost identical turnover frequency, very close to half of TOF for **1Pt-CZL**.

However, we can distinguish the effects of different platinum species by simple calculation (see Table S3), and the decided efficiencies for atoms, clusters, and particles are −0.029, +0.090, and +0.019 s^{-1} at 450 °C, respectively. It means that platinum oxide clusters (Pt_xO_y), with average size from subnanometer to 2−3 nm, play an essential role for the oxidation of methane; metallic Pt particles are probably active species, but their large-size characteristics impair the platinum efficiency; while ionic platinum single atoms show negative effect for the catalytic reaction in this work. Therefore, the Pt concentration has been optimized at 1 at. % with a summit on the percentage of ultrafine platinum oxide clusters.

5. CONCLUSIONS

In this work, low-concentration (0.5−2 at. %) platinum-doped ceria−zirconia−lanthana catalysts with high thermal and reaction stability were prepared by a simple impregnation method. The as-calcined samples showed good catalytic performance for the oxidation of methane up to 650 °C, and the highest reaction rate and the efficiency of platinum were observed for 1 at. % Pt loading. The aberration-corrected HAADF-STEM and XANES/EXAFS results identified that (1) ultrafine platinum oxide clusters play an essential for the oxidation of methane; (2) metallic Pt particles are also active species, while the large-sized ones lower the efficiency of platinum; and (3) ionic platinum single atoms do not help the methane oxidation reaction much.

■ ASSOCIATED CONTENT

Ⓢ Supporting Information

The Supporting Information is available free of charge on the ACS Publications website at DOI: 10.1021/acs.jpcc.7b07599.

> Testing conditions of Arrhenius plots for **Pt-CZL/CZL** samples, testing conditions for CO plus chemisorption, calculation on the efficiencies of different platinum species, nitrogen adsorption/desorption isotherms, BJH pore size distributions of fresh **Pt-CZL/CZL** samples, H_2-TPR profiles, integrated peak areas as a function of platinum concentrations for **Pt-CZL/CZL** samples, TEM images of used **Pt-CZL** samples, aberration-corrected HAADF-STEM images of fresh **1Pt-CZL** samples, diameter histograms on platinum clusters of fresh **Pt-CZL** samples, k^3-weighted EXAFS data in k-space of **Pt-CZL**, and XRD patterns of **0.5Pt-CZL** samples after hydrogen reduction (PDF)

■ AUTHOR INFORMATION

Corresponding Authors

*E-mail: sirui@sinap.ac.cn.
*E-mail: jiacj@sdu.edu.cn.
*E-mail: cma@hnu.edu.cn.

ORCID Ⓞ

Chun-Jiang Jia: 0000-0002-4254-5100
Ming-Xing Li: 0000-0003-0000-9876

Notes

The authors declare no competing financial interest.

■ REFERENCES

(1) Oh, S. H.; Bera, P. J.; Siewert, R. M. Methane Oxidation over Alumina-Supported Noble Metal Catalysts with and without Cerium Additives. *J. Catal.* **1991**, *132*, 287−301.

(2) Miao, S. J.; Deng, Y. Q. Au-Pt/Co3O4 Catalyst for Methane Combustion. *Appl. Catal., B* **2001**, *31*, L1−L4.

(3) Niwa, M.; Awano, K.; Murakami, Y. Activity of Supported Platinum Catalysts for Methane Oxidation. *Appl. Catal.* **1983**, *7*, 317−325.

(4) Becker, E.; Carlsson, P.-A.; Skoglundh, M. Methane Oxidation over Alumina and Ceria Supported Platinum. *Top. Catal.* **2009**, *52*, 1957−1961.

(5) Chen, C.; Yeh, Y.-H.; Cargnello, M.; Murray, C. B.; Fornasiero, P.; Gorte, R. J. Methane Oxidation on Pd@ZrO2/Si-Al2O3 is Enhanced by Surface Reduction of ZrO2. *ACS Catal.* **2014**, *4*, 3902−3909.

(6) Ma, Z. N.; Ouzilleau, P.; Trevisanut, C.; Neagoe, C.; Lotfi, S.; Boffito, D. C.; Patience, G. S. Partial Oxidation of Methane to Syngas over Pt/Rh/MgO Catalyst Supported on FeCr alloy Woven Fibre. *Can. J. Chem. Eng.* **2016**, *94*, 642−649.

(7) Wu, Z. X.; Deng, J. G.; Liu, Y. X.; Xie, S. H.; Jiang, Y.; Zhao, X. T.; Yang, J.; Arandiyan, H.; Guo, G. S.; Dai, H. X. Three-Dimensionally Ordered Mesoporous Co3O4-Supported Au-Pd Alloy Nanoparticles: High-Performance Catalysts for Methane Combustion. *J. Catal.* **2015**, *332*, 13−24.

(8) Ren, Z.; Botu, V.; Wang, S. B.; Meng, Y. T.; Song, W. Q.; Guo, Y. B.; Ramprasad, R.; Suib, S. L.; Gao, P. X. Monolithically Integrated Spinel MxCo3−xO4 (M = Co, Ni, Zn) Nanoarray Catalysts: Scalable Synthesis and Cation Manipulation for Tunable Low-Temperature CH4 and CO Oxidation. *Angew. Chem., Int. Ed.* **2014**, *53*, 7223−7227.

(9) Ruckenstein, E.; Wang, H. Y. Combined Catalytic Partial Oxidation and CO2 Reforming of Methane over Supported Cobalt Catalysts. *Catal. Lett.* **2001**, *73*, 2−4.

(10) Tanasoi, S.; Tanchoux, N.; Urdă, A.; Tichit, D.; Săndulescu, I.; Fajula, F.; Marcu, I.-C. New Cu-Based Mixed Oxides Obtained from LDH Precursors, Catalysts for Methane Total Oxidation. *Appl. Catal., A* **2009**, *363*, 135−142.

(11) Yisup, N.; Cao, Y.; Feng, W.-L.; Dai, W.-L.; Fan, K.-N. Catalytic Oxidation of Methane over Novel Ce-Ni-O Mixed Oxide Catalysts Prepared by Oxalate Gel-Coprecipitation. *Catal. Lett.* **2005**, *99*, 207−213.

(12) Cargnello, M.; Jaén, J. J. D.; Garrido, J. C. H.; Bakhmutsky, K.; Montini, T.; Gamez, J. J. C.; Gorte, R. J.; Fornasiero, P. Exceptional Activity for Methane Combustion over Modular Pd@CeO2 Subunits on Functionalized Al2O3. *Science* **2012**, *337*, 713−717.

(13) Gélin, P.; Urfels, L.; Primet, M.; Tena, E. Complete Oxidation of Methane at Low Temperature over Pt and Pd Catalysts for the Abatement of Lean-Burn Natural Gas Fuelled Vehicles Emissions: Influence of Water and Sulphur Containing Compounds. *Catal. Today* **2003**, *83*, 45−57.

(14) Tang, W.; Hu, Z. P.; Wang, M. J.; Stucky, G. D.; Metiu, H.; McFarland, E. W. Methane Complete and Partial Oxidation Catalyzed by Pt-Doped CeO_2. *J. Catal.* **2010**, *273*, 125−137.

(15) Beck, I. E.; Bukhtiyarov, V. I; Pakharukov, I. Y.; Zaikovsky, V. I.; Kriventsov, V. V.; Parmon, V. N. Platinum Nanoparticles on Al_2O_3: Correlation Between the Particle Size and Activity in Total Methane Oxidation. *J. Catal.* **2009**, *268*, 60−67.

(16) Persson, K.; Ersson, A.; Colussi, S.; Trovarelli, A.; Järås, S. G. Catalytic Combustion of Methane over Bimetallic Pd-Pt Catalysts: The Influence of Support Materials. *Appl. Catal., B* **2006**, *66*, 175−185.

(17) Pakulska, M. M.; Grgicak, C. M.; Giorgi, J. B. The Effect of Metal and Support Particle Size on NiO/CeO_2 and NiO/ZrO_2 Catalyst Activity in Complete Methane Oxidation. *Appl. Catal., A* **2007**, *332*, 124−129.

(18) Zhao, Y.-X.; Li, Z.-Y.; Yuan, Z.; Li, X.-N.; He, S.-G. Thermal Methane Conversion to Formaldehyde Promoted by Single Platinum Atoms in $PtAl_2O_4^-$ Cluster Anions. *Angew. Chem.* **2014**, *126*, 9636−9640.

(19) Psofogiannakis, G.; St-Amant, A.; Ternan, M. Methane Oxidation Mechanism on Pt(111): A Cluster Model DFT Study. *J. Phys. Chem. B* **2006**, *110*, 24593−24605.

(20) Arandiyan, H.; Dai, H. X.; Ji, K. M.; Sun, H. Y.; Li, J. H. Pt Nanoparticles Embedded in Colloidal Crystal Template Derived 3D Ordered Macroporous $Ce_{0.6}Zr_{0.3}Y_{0.1}O_2$: Highly Efficient Catalysts for Methane Combustion. *ACS Catal.* **2015**, *5*, 1781−1793.

(21) Hicks, R. F.; Qi, H. H.; Young, M. L.; Lee, R. G. Structure Sensitivity of Methane Oxidation over Platinum and Palladium. *J. Catal.* **1990**, *122*, 280−294.

(22) Si, R.; Flytzani-Stephanopoulos, M. Shape and Crystal-Plane Effects of Nanoscale Ceria on the Activity of $Au-CeO_2$ Catalysts for the Water-Gas Shift Reaction. *Angew. Chem., Int. Ed.* **2008**, *47*, 2884−2887.

(23) Gupta, A.; Waghmare, U. V.; Hegde, M. S. Correlation of Oxygen Storage Capacity and Structural Distortion in Transition-Metal-, Noble-Metal-, and Rare-Earth-Ion-Substituted CeO_2 from First Principles Calculation. *Chem. Mater.* **2010**, *22*, 5184−5198.

(24) Du, P.-P.; Hu, X.-C.; Wang, X.; Ma, C.; Du, M.; Zeng, J.; Jia, C.-J.; Huang, Y.-Y.; Si, R. Synthesis and Metal-Support Interaction of Subnanometer Copper-Palladium Bimetallic Oxide Clusters for Catalytic Oxidation of Carbon Monoxide. *Inorg. Chem. Front.* **2017**, *4*, 668−674.

(25) Yang, Q.; Fu, X.-P.; Jia, C.-J.; Ma, C.; Wang, X.; Zeng, J.; Si, R.; Zhang, Y.-W.; Yan, C.-H. Structural Determination of Catalytically Active Subnanometer Iron Oxide Clusters. *ACS Catal.* **2016**, *6*, 3072−3082.

(26) Kašpar, J.; Fornasiero, P.; Hickey, N. Automotive Catalytic Converters: Current Status and Some Perspectives. *Catal. Today* **2003**, *77*, 419−449.

(27) Si, R.; Zhang, Y.-W.; Wang, L.-M.; Li, S.-J.; Lin, B.-X.; Chu, W.-S.; Wu, Z.-Y.; Yan, C.-H. Enhanced Thermal Stability and Oxygen Storage Capacity for $Ce_xZr_{1-x}O_2$ (x = 0.4−0.6) Solid Solutions by Hydrothermally Homogenous Doping of Trivalent Rare Earths. *J. Phys. Chem. C* **2007**, *111*, 787−794.

(28) Cheng, N. C.; Stambula, S.; Wang, D.; Banis, M. N.; Liu, J.; Riese, A.; Xiao, B. W.; Li, R. Y.; Sham, T.-K.; Liu, L.-M.; et al. Platinum Single-Atom and Cluster Catalysis of the Hydrogen Evolution Reaction. *Nat. Commun.* **2016**, *7*, 13638.

(29) Nilsson, J.; Carlsson, P.-A.; Fouladvand, S.; Martin, N. M.; Gustafson, J.; Newton, M. A.; Lundgren, E.; Grönbeck, H.; Skoglundh, M. Chemistry of Supported Palladium Nanoparticles during Methane Oxidation. *ACS Catal.* **2015**, *5*, 2481−2489.

(30) Li, Y.; Zakharov, D.; Zhao, S.; Tappero, R.; Jung, U.; Elsen, A.; Baumann, Ph.; Nuzzo, R. G.; Stach, E. A.; Frenkel, A. I. Complex Structural Dynamics of Nanocatalysts Revealed in Operando Conditions by Correlated imaging and Spectroscopy Probes. *Nat. Commun.* **2015**, *6*, 7583.

(31) Sun, Y.; Frenkel, A. I.; Isseroff, R.; Shonbrun, C.; Forman, M.; Shin, K.; Koga, T.; White, H.; Zhang, L. H.; Zhu, Y. M.; et al. Characterization of Palladium Nanoparticles by Using X-ray Reflectivity, EXAFS, and Electron Microscopy. *Langmuir* **2006**, *22*, 807−816.

(32) Langford, J. I. Powder Pattern Programs. *J. Appl. Crystallogr.* **1971**, *4*, 259−260.

(33) Langford, J. I. The Accuracy of Cell Dimensions Determined by Cohen's Method of Least Squares and the Systematic Indexing of Powder Data. *J. Appl. Crystallogr.* **1973**, *6*, 190−196.

(34) Barrett, E. P.; Joyner, L. G.; Halenda, P. H. The Determination of Pore Volume and Area Distributions in Porous Substances. I. Computations from Nitrogen Isotherms. *J. Am. Chem. Soc.* **1951**, *73*, 373−380.

(35) Yu, H.-S.; Wei, X.-J.; Li, J.; Gu, S.-Q.; Zhang, S.; Wang, L.-H.; Ma, J.-Y.; Li, L.-N.; Gao, Q.; Si, R.; et al. The XAFS Beamline of SSRF. *Nucl. Sci. Technol.* **2015**, *26*, 050102.

(36) Frenkel, A. I.; Wang, Q.; Marinkovic, N.; Chen, J. G.; Barrio, L.; Si, R.; Camara, A. L.; Estrella, A. M. J.; Rodriguez, A.; Hanson, J. C. Combining X-ray Absorption and X-ray Diffraction Techniques for in Situ Studies of Chemical Transformations in Heterogeneous Catalysis: Advantages and Limitations. *J. Phys. Chem. C* **2011**, *115*, 17884−17890.

(37) Stakheev, A. Y.; Batkin, A. M.; Teleguina, N. S.; Bragina, G. O.; Zaikovsky, V. I.; Prosvirin, I. P.; Khudorozhkov, A. K.; Bukhtiyarov, V. I. Particle Size Effect on CH_4 Oxidation Over Noble Metals: Comparison of Pt and Pd Catalysts. *Top. Catal.* **2013**, *56*, 306−310.

(38) Lee, S.; Seo, J.; Jung, W. C. Sintering-Resistant $Pt@CeO_2$ Nanoparticles for High-Temperature Oxidation Catalysis. *Nanoscale* **2016**, *8*, 10219−10228.

(39) Wang, X.; Du, L.-Y.; Du, M.; Ma, C.; Zeng, J.; Jia, C.-J.; Si, R. Catalytically Active Ceria-Supported Cobalt-Manganese Oxide Nano-catalysts for Oxidation of Carbon Monoxide. *Phys. Chem. Chem. Phys.* **2017**, *19*, 14533−14542.

(40) Ke, J.; Zhu, W.; Jiang, Y.-Y.; Si, R.; Wang, Y.-J.; Li, S.-C.; Jin, C.-H.; Liu, H.-C.; Song, W.-G.; Yan, C.-H.; et al. Strong Local Coordination Structure Effects on Subnanometer PtO_x Clusters over CeO_2 Nanowires Probed by Low-Temperature CO Oxidation. *ACS Catal.* **2015**, *5*, 5164−5173.

(41) Chen, Q.-Y.; Li, N.; Luo, M.-F.; Lu, J.-Q. Catalytic Oxidation of Dichloromethane over $Pt/CeO_2-Al_2O_3$ Catalysts. *Appl. Catal., B* **2012**, *127*, 159−166.

(42) Sing, K. S. W.; Everett, D. H.; Haul, R. A. W.; Moscou, L.; Pierotti, R. A.; Rouquerol, J.; Siemieniewska, T. Reporting Physisorption Data for Gas/Solid Systems with Special Reference to the Determination of Surface Area and Porosity. *Pure Appl. Chem.* **1985**, *57*, 603−619.

(43) Lee, E.; Manthiram, A. One-Step Reverse Microemulsion Synthesis of $Pt-CeO_2/C$ Catalysts with Improved Nanomorphology and Their Effect on Methanol Electrooxidation Reaction. *J. Phys. Chem. C* **2010**, *114*, 21833−21849.

(44) Kamiuchi, N.; Haneda, M.; Ozawa, M. CO Oxidation over Pt/Ce−Zr Oxide Catalysts with Low Content of Platinum and Cerium Components. *Catal. Today* **2013**, *201*, 79−84.

(45) Weber, W. H.; Hass, K. C.; McBride, J. R. Raman Study of CeO_2: Second-Order Scattering, Lattice Dynamics, and Particle-Size Effects. *Phys. Rev. B: Condens. Matter Mater. Phys.* **1993**, *48*, 178−185.

(46) Si, R.; Zhang, Y.-W.; Xiao, C.-X.; Li, S.-J.; Lin, B.-X.; Kou, Y.; Yan, C.-H. Non-Template Hydrothermal Route Derived Mesoporous $Ce_{0.2}Zr_{0.8}O_2$ Nanosized Powders with Blue-Shifted UV Absorption and High CO Conversion Activity. *Phys. Chem. Chem. Phys.* **2004**, *6*, 1056−1063.

(47) Lee, Y. J.; He, G. H.; Akey, A. J.; Si, R.; Flytzani-Stephanopoulos, M.; Herman, I. P. Raman Analysis of Mode Softening in Nanoparticle $CeO_{2-\delta}$ and $Au-CeO_{2-\delta}$ during CO Oxidation. *J. Am. Chem. Soc.* **2011**, *133*, 12952−12955.

(48) Vita, A.; Cristiano, G.; Italiano, C.; Pino, L.; Specchia, S. Syngas Production by Methane Oxy-Steam Reforming on Me/CeO_2 (Me = Rh, Pt, Ni) Catalyst Lined on Cordierite Monoliths. *Appl. Catal., B* **2015**, *162*, 551−563.

(49) Jones, J.; Xiong, H. F.; DeLaRiva, A. T.; Peterson, E. J.; Pham, H.; Challa, S. R.; Qi, G. S.; Oh, S.; Wiebenga, M. H.; Hernández, X. I. P.; et al. Thermally Stable Single-Atom Platinum-on-Ceria Catalysts Via Atom Trapping. *Science* **2016**, *353*, 150−154.

(50) Nagai, Y.; Hirabayashi, T.; Dohmae, K.; Takagi, N.; Minami, T.; Shinjoh, H.; Matsumoto, S. Sintering Inhibition Mechanism of Platinum

Supported on Ceria-Based Oxide and Pt-Oxide-Support Interaction. *J. Catal.* **2006**, *242*, 103−109.

(51) Bera, P.; Priolkar, K. R.; Gayen, A.; Sarode, P. R.; Hegde, M. S.; Emura, S.; Kumashiro, R.; Jayaram, V.; Subbanna, G. N. Ionic Dispersion of Pt over CeO$_2$ by the Combustion Method: Structural Investigation by XRD, TEM, XPS, and EXAFS. *Chem. Mater.* **2003**, *15*, 2049−2060.

(52) Frenkel, A. I.; Hills, C. W.; Nuzzo, R. G. A View from the Inside: Complexity in the Atomic Scale Ordering of Supported Metal Nanoparticles. *J. Phys. Chem. B* **2001**, *105*, 12690−12703.

(53) Tanabe, T.; Nagai, Y.; Hirabayashi, T.; Takagi, N.; Dohmae, K.; Takahashi, N.; Matsumoto, S.; Shinjoh, H.; Kondo, J. N.; Schouten, J. C.; et al. Low Temperature CO Pulse Adsorption for the Determination of Pt Particle Size in a Pt/Cerium-based Oxide Catalyst. *Appl. Catal., A* **2009**, *370*, 108−113.

(54) Kinnunen, N. M.; Hirvi, J. T.; Suvanto, M.; Pakkanen, T. A. Methane Combustion Activity of Pd-PdO$_x$-Pt/Al$_2$O$_3$ Catalyst: The Role of Platinum Promoter. *J. Mol. Catal. A: Chem.* **2012**, *356*, 20−28.